Parallel transmission 2D RARE imaging at 7T with transmit field inhomogeneity mitigation and local SAR control

Magnetic Resonance Imaging 93 (2022) 87–96

Contents lists available at ScienceDirect

Magnetic Resonance Imaging

journal homepage: www.elsevier.com/locate/mri

Parallel transmission 2D RARE imaging at 7T with transmit field inhomogeneity mitigation and local SAR control

Filiz Yetisir [a,*], Benedikt A. Poser [b], P. Ellen Grant [a,c,d], Elfar Adalsteinsson [e,f,g], Lawrence L. Wald [d,f,h], Bastien Guerin [d,h]

[a] Fetal-Neonatal Neuroimaging & Developmental Science Center, Boston Children's Hospital, Harvard Medical School, 300 Longwood Avenue, Boston, MA 02115, USA
[b] Department of Cognitive Neuroscience, Faculty of Psychology and Neuroscience, Maastricht University, Universiteitssingel 40, 6229 ER Maastricht, the Netherlands
[c] Department of Pediatrics, Harvard Medical School, 25 Shattuck Street, Boston, MA 02115, USA
[d] Department of Radiology, Harvard Medical School, 25 Shattuck Street, Boston, MA 02115, USA
[e] Department of Electrical Engineering and Computer Science, Massachusetts Institute of Technology, 77 MA Avenue, Cambridge, MA 02139, USA
[f] Harvard-MIT Division of Health Sciences and Technology, Massachusetts Institute of Technology, 77 MA Avenue, Cambridge, MA 02139, USA
[g] Institute for Medical Engineering and Science, Massachusetts Institute of Technology, 77 MA Avenue, Cambridge, MA 02139, USA
[h] Athinoula A. Martinos Center for Biomedical Imaging, MA General Hospital, 149 13th Street, Charlestown, MA 02129, USA

A R T I C L E I N F O

Keywords:
Ultra-high field MRI
Parallel transmission
RARE
turbo spin echo
Local SAR
RF pulse design

A B S T R A C T

Purpose: We develop and test a parallel transmit (pTx) pulse design framework to mitigate transmit field inhomogeneity with control of local specific absorption rate (SAR) in 2D rapid acquisition with relaxation enhancement (RARE) imaging at 7T.
Methods: We design large flip angle RF pulses with explicit local SAR constraints by numerical simulation of the Bloch equations. Parallel computation and analytical expressions for the Jacobian and the Hessian matrices are employed to reduce pulse design time. The refocusing-excitation "spokes" pulse pairs are designed to satisfy the Carr-Purcell-Meiboom-Gill (CPMG) condition using a combined magnitude least squares-least squares approach.
Results: In a simulated dataset, the proposed approach reduced peak local SAR by up to 56% for the same level of refocusing uniformity error and reduced refocusing uniformity error by up to 59% (from 32% to 7%) for the same level of peak local SAR compared to the circularly polarized birdcage mode of the pTx array. Using explicit local SAR constraints also reduced peak local SAR by up to 46% compared to an RF peak power constrained design. The excitation and refocusing uniformity error were reduced from 20%–33% to 4%–6% in single slice phantom experiments. Phantom experiments demonstrated good agreement between the simulated excitation and refocusing uniformity profiles and experimental image shading.
Conclusion: PTx-designed excitation and refocusing CPMG pulse pairs can mitigate transmit field inhomogeneity in the 2D RARE sequence. Moreover, local SAR can be decreased significantly using pTx, potentially leading to better slice coverage, enabling larger flip angles or faster imaging.

1. Introduction

The greater signal-to-noise and contrast-to-noise ratio provided by MRI at 7Tesla (T) has been shown to provide potential diagnostic advantages for epilepsy, multiple sclerosis, Alzheimer's disease, cancer, cerebrovascular disease, and other neurological disorders [1–6]. However, the advantages of Ultra High Field (UHF) MRI are partially diminished by flip angle (FA) and refocusing nonuniformity across the image [7–9]. These arise from the B_1^+ field inhomogeneity of the radiofrequency (RF) transmission. In addition, SAR limitations at UHF [7,8,10] impose reduced slice coverage and FA or longer scan times.

Slice selective (2D) rapid imaging of refocused echoes (RARE) [11], also known as turbo or fast spin echo (TSE, FSE), is one of the most common MR imaging techniques used in the clinic. RARE applies multiple, consecutive refocusing RF pulses to collect many k-space lines following a single excitation pulse. This dramatically increases the amount of data acquired in a single repetition time (TR), increases acquisition efficiency and reduces total acquisition time. Increased SAR at 7T is especially limiting for RARE imaging due to its use of a train of high RF power refocusing pulses [1,3]. RARE at 7T also suffers from

* Corresponding author at: Department of Newborn Medicine, Boston Children's Hospital, 300 Longwood Avenue, BCH 3181, Boston, MA 02115, USA.
E-mail address: filiz.yetisir@childrens.harvard.edu (F. Yetisir).

https://doi.org/10.1016/j.mri.2022.08.006
Received 4 May 2022; Received in revised form 15 July 2022; Accepted 2 August 2022
Available online 5 August 2022
0730-725X/

spatial variations in the applied B_1^+ field. This directly effects the magnetization produced by the excitation pulse (the "90-degree pulse") by locally reducing it from the optimal full excitation. Similarly, variations in B_1^+ modulate the efficiency of traditional refocusing pulses. Hence, the widespread adoption of 7T MRI has been challenging in clinical and clinical research settings heavily relying on T_2 contrast.

Several solutions have been developed to address the transmit field inhomogeneity and increased SAR at 7T. Slice-selective adiabatic RF pulses provide great immunity to transmit field inhomogeneity [12–14]; however, they usually require a longer pulse duration or more RF power than conventional RF pulses [13–16]. Variable-rate selective excitation (VERSE) method [17] as well as low- and variable-flip-angle echo trains designed by the extended phase algorithm [18,19] have been proposed as effective ways of reducing SAR. However, transmit field inhomogeneity is not directly addressed by these approaches. More recently, dielectric pads have been used to regionally manipulate the B_1^+ fields improving homogeneity and, as indicated by a few authors, even reducing SAR [20–26]. This helpful passive shimming approach is synergistic with additional explicitly calculated subject specific mitigation approaches such as parallel RF transmission [27–29]. Time interleaved acquisition of modes (TIAMO) method mitigates signal voids due to B_1^+ field inhomogeneities by combining images acquired with two different modes of excitation using parallel imaging techniques [30]. However, this approach slightly increases SAR compared to the standard mode and comes with a certain SNR or scan time penalty.

Parallel transmission (pTx) technology allows RF energy to be simultaneously transmitted by multiple independently controlled elements in a transmit array and provides the ability to address both transmit field inhomogeneity and SAR challenges associated with 7T MRI [27–29]. To this end, several methods have been proposed to design pTx RF pulses. Most of these methods, however, accommodate only small FA designs [27,28,31–39], are non-selective [35,38–46] or 2D or 3D selective [33,47–50], or do not explicitly control local SAR [27,31,33–36,38,40,43,46–48,50–52], aspects that are crucial for fast 2D RARE imaging.

Designing pTx RF pulses for RARE imaging moreover presents an additional challenge since the Carr-Purcell-Meiboom-Gill (CPMG) condition [53,54] must be satisfied in order to minimize the effect of imperfect refocusing. Imposing the CPMG condition in the standard mode of operation is straightforward, excitation and refocusing pulses have a 90° phase offset. However, it is in general advantageous to utilize a different mode of the array for the two pulses in order to mitigate varying B_1^+ patterns and reduce local SAR. In this case the CPMG condition cannot be maintained at all spatial locations by a simple phase offset. Hence, CPMG condition needs to be enforced in the pulse design when using pTx. As a result of this complication, most large FA pTx methods have been applied to gradient echo [55] or spin echo [46,52,56–59] sequences but not to RARE.

In order to satisfy the CPMG condition with pTx pulses, Xu et al. [60] proposed a joint design of the excitation and refocusing pulses for a spiral excitation k-space trajectory and demonstrated the performance of this approach using Bloch simulations. Massire et al. [43] imposed the CPMG condition in their design of non-selective kT-point pulses using the gradient ascent pulse engineering algorithm [46]. Alternatively, Sbrizzi et al. [61] optimized signal intensity in slice selective and nonselective RARE imaging using the extended phase algorithm approach and designing different RF shim settings for each refocusing pulse. This approach avoids having to explicitly impose the CPMG constraint as the signal is directly optimized and the CPMG condition is naturally satisfied, at the expense of additional computation time. In summary, previous studies exist which satisfy the CPMG condition in RARE imaging, however, they lack either slice-selectivity [43], experimental validation [60], multi-spoke pulses [61], or explicit local SAR constraints [60].

In this study, we propose an efficient pTx pulse design algorithm capable of designing multi-spoke excitation and refocusing pulses which satisfy the CPMG condition, and experimentally demonstrate the performance of the designed pulses in phantom experiments using a pTx-enabled slice-selective RARE imaging sequence. We build on our previous local SAR-constrained pulse design algorithm [42,62] by adding enforcement of the CPMG condition. The RF pulse design forward model is based on the spin domain formulation of the Bloch equations, and therefore accommodates large FA. In order to improve convergence and speed up the computation, we provide the exact analytical Jacobian (1st derivative) and an approximation of the Hessian matrix (2nd derivatives) of the objective function and the constraints to the optimizer. In addition, we use a graphics processing unit (GPU). Although the excitation and refocusing pulse designs are not treated as a true joint optimization as in Xu et al. [60], they must be considered together. We study different approaches, including either a simple least-squares (i.e., sensitive to the phase) or magnitude least-squares optimization of the refocusing pulse followed by a least-squares design of the excitation pulse with enforcement of the CPMG phase condition using a similar approach to that implemented for non-selective pulses in Massire et al. [43]. Additionally, we analyze 1- and 2-spoke designs for both pulses. Finally, we demonstrate the image shading and image artifacts performance of our approach in phantom experiments.

2. Methods

2.1. Local SAR constrained slice selective large Flip angle pulse design

We design large FA pTx pulses based on our previous approach [42,62]. The effect of the RF pulse on the magnetization (i.e., forward model) is calculated using the discretized Bloch dynamics in the spin domain [63]. In other words, each RF sample is associated with a spinor (α, β), where α and β are the Cayley-Klein parameters [63], and the effect of the entire pulse is represented by the multiplication of these spinors. For a "least-squares" design, we solve the following optimization:

$$\min_{x} \left\| \boldsymbol{y}(\boldsymbol{x}) - \boldsymbol{y}_{target} \right\|_2^2 \tag{1}$$

Subject to

$$DC \frac{1}{N} \sum_{i=1}^{N} \boldsymbol{b}(\boldsymbol{x})_i{}^{\boldsymbol{H}} \boldsymbol{S}_v \boldsymbol{b}(\boldsymbol{x})_i < LSAR_{max} \forall v \in V$$

$$DC \frac{1}{N} \sum_{i=1}^{N} \boldsymbol{b}(\boldsymbol{x})_i{}^{\boldsymbol{H}} \boldsymbol{S}_g \boldsymbol{b}(\boldsymbol{x})_i < GSAR_{max}$$

$$DC \frac{1}{N} \sum_{i=1}^{N} \frac{\left| b(\boldsymbol{x})_{c,i} \right|^2}{8Z_0} < P_{ave,max} \ \ \forall c \in \{1, \ldots, C\}$$

$$\left| b(\boldsymbol{x})_{c,i} \right| \langle x_{max} \forall c \in \{1, \ldots, C\} \ and \ \forall i \in \{1, \ldots, N\}$$

where $\boldsymbol{x}$ is a vector including the complex spoke weights for all channels (unit in volts), $\boldsymbol{y}(\boldsymbol{x})$ is the spatial profile (excitation or refocusing) of the RF pulse, $\boldsymbol{y}_{target}$ is the target spatial profile of the RF pulse, DC is the duty cycle, N is the number of discretized points in the RF pulse, $\boldsymbol{b}(\boldsymbol{x})_i$ (a vector of length C where C is the number of transmit channels) is the RF pulse at time i which is determined by $\boldsymbol{x}$ and the RF sub-pulse shape, $\boldsymbol{S}_v$ is the virtual observation point (VOP) matrix [64], $LSAR_{max}$ is the peak 10 g averaged local SAR (pSAR10g) limit, V is the set of all VOPs, $\boldsymbol{S}_g$ is the global SAR matrix, $GSAR_{max}$ is the global SAR limit, c is the transmit channel number, $b(\boldsymbol{x})_{c,\,i}$ is the value of the RF pulse at channel c at time i, Z_0 is the reference impedance of the coil, $P_{ave,\,max}$ is the average power limit per channel, x_{max} is the RF peak voltage limit. The factor 8 in the average power calculation is because half the source voltage is across the coil port when the power is matched and the voltage quantities are in amplitude rather than RMS. If the coil port voltage is used, then a factor of 2 is used.

For slice selectivity, we use spokes pulses [65,66] with Hamming windowed sinc sub-pulses. While the time discretization step for the Bloch simulation is 10 μs to adequately account for off-resonance effects, only the complex amplitudes of the sub-pulses (or the spokes) need to be solved for in the optimization. Therefore, $\boldsymbol{x}$ includes $C*S$ complex elements, where S is the number of spokes. In order to improve the efficiency of our pulses and overcome RF peak voltage limitations, we have found it helpful to pre-VERSE our sub-pulse profiles (minimum-time VERSE [17]) before the optimization process. This has the advantage that the pulse design optimization occurs after the VERSE step and can therefore account for off-resonance effects introduced by the VERSE method. In order to increase robustness to timing miscalibrations between the RF and gradient subsystem as well as eddy current effects, we employ a monopolar slice selection scheme for 2-spoke pulses whereby each spoke is played out with the same gradient polarity [67–69].

The minimization in Eq. (1) is solved iteratively where $\boldsymbol{y}(\boldsymbol{x})$ is calculated from the Cayley-Klein parameters of the RF pulse at every iteration. The Cayley-Klein parameters are computed from a numerical simulation of the Bloch equations [63]. Both $\boldsymbol{y}(\boldsymbol{x})$ and $\boldsymbol{y}_{target}$ depend on whether the pulse is an excitation or refocusing pulse [63]. For an excitation pulse with an initial magnetization $[0\ 0\ M_0]^T$:

$$\begin{aligned} \boldsymbol{y}(\boldsymbol{x}) &= 2\boldsymbol{\alpha}^*(\boldsymbol{x})\boldsymbol{\beta}(\boldsymbol{x}) \\ \boldsymbol{y}_{target} &= sin(\boldsymbol{\theta})e^{i\boldsymbol{\varphi}} \end{aligned} \tag{2}$$

where $\boldsymbol{\theta}$ is the target FA and $\boldsymbol{\varphi}$ is the target phase profile at all spatial locations. For a refocusing pulse with a target FA of 180° and crusher gradients played before and after the refocusing pulse:

$$\begin{aligned} \boldsymbol{y}(\boldsymbol{x}) &= \boldsymbol{\beta}^2(\boldsymbol{x}) \\ \boldsymbol{y}_{target} &= -e^{i2\boldsymbol{\varphi}} \end{aligned} \tag{3}$$

where $\boldsymbol{\varphi}$ is the target refocusing axis profile at all spatial locations. These expressions are complex and are therefore suitable for both least-squares (LS) and magnitude least-squares (MLS) optimization [31] (for MLS, the magnitude of $\boldsymbol{y}(\boldsymbol{x})$ and $\boldsymbol{y}_{target}$ are used in Eq. (1). The nonlinear constrained optimization function *fmincon* in MATLAB (Natick, MA, USA) was used with an interior-point algorithm to solve Eq. (1).

The minimization problem in Eq. (1) is nonconvex, therefore it is crucial to initialize it properly. For this purpose, we first design a small FA RF pulse using the small tip angle approximation approach [28,32,70] for a target FA of 30° which we then scale to the actual target FA. Note that the local SAR, global SAR and RF peak power limits are scaled appropriately in the small FA pulse design so that when the pulses are scaled up to the target FA, they still satisfy the hardware and regulatory limits.

In order to generate the VOP matrices in Eq. (1), we modelled and simulated our in-house built 8-channel loop array (Supporting Information Fig. S1) using the electromagnetic modeling suite HFSS (Ansys Inc., Canonsburg, PA, USA). The coil model was loaded with the 33-tissue types Ansys male body model (Supporting Information Fig. S1) with a head centered position. SAR matrices were computed from the simulated electric fields with a resolution of 2 mm and subsequently compressed using the VOP algorithm [64] resulting in 739 VOP matrices (5% overestimation factor).

The excitation or refocusing uniformity error was quantified for LS designs by the normalized root mean square error (NRMSE) as follows:

$$NRMSE\ (\%) = \frac{\left\|\boldsymbol{y}(\boldsymbol{x}) - \boldsymbol{y}_{target}\right\|_2}{\left\|\boldsymbol{y}_{target}\right\|_2} * 100 \tag{4}$$

For MLS designs, the magnitude of $\boldsymbol{y}(\boldsymbol{x})$ and $\boldsymbol{y}_{target}$ were used to calculate the normalized root magnitude mean square error (NRMMSE).

2.2. L-curves

L-curves were generated to evaluate the refocusing uniformity versus local SAR trade-off for 1- and 2-spoke pulses. This was done by varying the limits for peak local SAR ($LSAR_{max}$) or the peak RF voltage (x_{max}) and plotting the resulting $|\beta^2|$ uniformity error (NRMMSE) versus pSAR10g. These L-curves were generated only for refocusing pulses (designed with MLS) because most of the SAR in RARE imaging is generated by the train of refocusing pulses. The L-curve analysis used simulated B_1^+ fields and VOPs from the Ansys male body model and the numerical model of the in-house built 8 channel loop array (Supporting Information Fig. S1 and S2). An in-vivo off-resonance map acquired at isocenter was fitted inside the isocenter slice of the Ansys male body model to create an artificial off-resonance map. Additionally, we used Hamming windowed VERSEd sinc sub-pulses with a time bandwidth product (TBW) of 2.5, and a sub-pulse length of 1.5 ms for a slice thickness (ST) of 3 mm for the L-curves resulting in a total pulse duration of 2.5 ms and 4.8 ms for 1- and 2-spoke pulses. For 2-spokes pulses, the spoke locations were chosen to be (0,0,0) and (5,5,0).

The optimized pulses were then compared with the CP birdcage mode of operation of the pTx array (called in short CP mode), whereby the channels are driven in a fixed amplitude and phase relationship (all B_1^+ values in phase at the center of the FOV). For the CP mode, two variations are possible: "CP mode center" whereby pulses are scaled so that the FA at the center of the image reaches the target and "CP mode average" whereby pulses are scaled so that the average FA throughout the slice is equal to the target. For the L-curves, we generated two versions of the "CP mode average" where the sub-pulse length was either 1.5 ms (total RF transmission duration matched to 1-spoke pulses) or 3 ms (total RF transmission duration matched to 2-spoke pulses) since pulse-length directly affects pSAR10g. A duty cycle of 15% was assumed for all pulses in the L-curves and peak local SAR, head average SAR, average power per channel and peak voltage (at the source) per channel was limited by 10 W/kg, 3.2 W/kg, 10 W, 300 V (225 W peak power) respectively.

2.3. Reduction of computation time

The proposed large FA pulse design algorithm is an iterative optimization where every iteration requires multiplication of hundreds of spinors. Moreover, with explicit local SAR constraints, hundreds of constraints are added to the minimization which further increases the complexity of the optimization resulting in a computationally intensive process. Since pTx pulse design must be performed while the patient is inside the scanner unless pre-calculated RF pulses such as universal pulses [44] are used, long computation times, e.g. a few minutes per slice, are undesirable and usually unacceptable.

In order to accelerate the pulse design, we provide the Jacobian and an approximated version of the Hessian matrix of the objective and constraint functions to the minimizer. The Jacobian is computed analytically by derivation of the objective and constraint functions with respect to the unknowns, i.e., the real and imaginary parts of the spoke complex weights. Exact computation of the Hessian is prohibitive since this would require a double "for"-loop over the RF time points. This would result in a computation that is slower than the anticipated convergence improvement obtained by using the Hessian information. Instead, we provide an approximation of the Hessian that is easy to compute and still helps convergence. The key assumption is to set the off-resonance field to zero, which collapses all the spinors of each spoke and each gradient blip into a single spinor that is straightforward to compute. With this simplification, for example, for a single spoke pulse with a sub-pulse length of 1.5 ms and a gradient rewinder length of 0.5 ms, two spinors are used to represent the pulse instead of 200 (for time discretization step of 10 μs). Details of the Jacobian and the approximate Hessian matrix computation of the objective function in Eq. (1) are provided in the Supporting Information.

We implement parallel computation using a GPU (NVIDIA GeForce GTX 980 Ti, 2816 cores, 1000 MHz, 6144 MB) to compute the Jacobian and Hessian matrices. The GPU accelerated computation times were compared to those of a CPU (Intel(R) Core(TM) i7-6700K @4GHz, 4 cores, 8 logical processors) with a system memory of 64 GB. Note that the comparisons between CPU and GPU computations are difficult to generalize since they are specific to the hardware and software implementations used. The computation time analysis used simulated B_1^+ fields and the VOPs generated from the Ansys male body model and the numerical model of the in-house built pTx array (Supporting Information Figs. S1 and S2). Similar to the L-curve analysis, an artificial off-resonance map created from an in-vivo off-resonance map was included in pulse design computation time analysis. The RF pulse parameters, duty cycle as well as SAR, power and RF peak voltage limitations used in the L-curve analysis were also used for the pulse design computation time analysis. In order to reduce computation time, B_1^+ fields were down-sampled to a resolution of 4 × 4 mm^2 without a significant effect on the resulting $|\beta^2|$ profiles.

2.4. Design of refocusing-excitation pulse pairs for RARE imaging

The CPMG condition imposes a 90° phase shift between the excitation and the refocusing pulses. This condition must be satisfied at every location in the slice. One way to achieve this requirement for pTx pulses is to use the same target phase profile in the LS optimization when designing both excitation and refocusing pulses. We refer to this as the "LS-LS" approach. However, this precludes the ability to take advantage of the MLS design [31]. Hence, we first design the refocusing pulse using MLS and then design the excitation pulse using LS (the "MLS-LS" approach), similar to the approach in Massire et al. [43]. The target phase map of the LS-designed excitation pulse is set to that of the refocusing pulse's map to satisfy the CPMG condition. We chose to apply the MLS advantage to the refocusing pulse since it is the more challenging design problem and requires more RF power.

We simulated the spin echo signal for each excitation-refocusing pulse pair by dividing each voxel into 20 steps along x and y, concatenating the excitation and the refocusing pulses (after adding crusher gradients before and after the refocusing pulse), running a full Bloch simulation and summing the transverse signal right after the second crusher gradient along x and y inside the voxel. We ignored the relaxation effects in the spin echo signal simulation.

In addition, we calculated the slice profile of different pulses and the spin echo signal by running a full Bloch simulation for several points along the slice select direction (range = [−8 mm, 8 mm], step size = 0.4 mm). As a reference for the slice profile, small tip angle excitation pulses (FA = 30°) were also designed with pulse parameters (slice thickness, pulse duration, VERSE factor, etc.) matching to those of different 90° excitation and 180° refocusing pulses. The deviation of the resulting slice profiles for each in plane location (x, y) from an ideal slice profile was quantified using the following metric:

$$\textit{Slice profile error}\,(x,y)=\sum_{z}\|\,|SP(z)|-|SP_{ideal}(z)|\,\|_2 \tag{5}$$

where SP is the slice profile of a specific RF pulse or pulse pair and SP_{ideal} is the ideal rectangular slice profile for the given slice thickness. The slice profiles for different RF pulses and spin echo signals are then compared using the average and the standard deviation of the slice profile error (as defined in Eq.(5)) across the transverse plane.

2.5. Imaging experiments

All experiments were conducted on a 7T Magnetom scanner (Siemens, Erlangen, Germany) equipped with an 8 channel transmit array (VB17 step 2.3 software), maximum gradient amplitude of 70 mT/m and slew rate of 200 T/m/s. We used an in-house built transceiver loop array for the experiments (Supporting Information Fig. S1).

A pre-saturation based turbo flash sequence [71] was used to acquire transmit field maps (resolution = 3.1 × 3.1 mm^2, ST = 5 mm, acquisition time (TA) = 3:21 min) and a double echo gradient echo (GRE) sequence was used to acquire a ΔB_0 field map [72,73] (resolution = 3.1 × 3.1 mm^2, ST = 5 mm, TA = 1:42 min). We tested the pTx pulses experimentally using a pTx-enabled RARE sequence which we modified from the Siemens product RARE sequence. The sequence allows loading channel-specific RF pulses as well as arbitrary gradient waveforms. Both the RF and gradient pulses were specified on a 10 μs raster.

The phantom experiments used a 3D-printed 3-compartment (brain, bone, everything else) 3% agar head phantom created using the approach described in [74]. Transmit field maps and off-resonance map for the phantom experiments are shown in Fig. 1. The pulse design for the phantom experiments did not utilize SAR constraints in order to demonstrate the minimum achievable excitation or refocusing uniformity error. Image artifacts introduced by the repeated application of refocusing pulses in RARE were assessed by comparison with a single spin echo (SE) sequence. Artifact levels were quantified by:

$$\textit{Artifact level}\,(\%)=\frac{1}{N}*\sum_{i\in m}\frac{\boldsymbol{Img}_{SE}(i)-\boldsymbol{Img}_{RARE}(i)}{\boldsymbol{Img}_{SE}(i)}*100 \tag{6}$$

where $\boldsymbol{Img}_{SE}$ and $\boldsymbol{Img}_{RARE}$ are the single spin echo and RARE images obtained with the same refocusing-excitation pulse pair, $\boldsymbol{m}$ is the image mask drawn manually to exclude the outer layer of the phantom and N is the total number of nonzero elements inside $\boldsymbol{m}$.

The following imaging parameters were used for single spin echo and RARE phantom experiments: FOV = 200 × 200 mm^2, matrix size = 256 × 256, nominal resolution = 0.8 × 0.8 mm^2, ST = 5 mm, TR = 3 s, TE = 11–14 ms, bandwidth per pixel = 130 Hz, number of averages = 1, ETL = 1 for single spin echo (251 shots) and ETL = 7 for RARE (36 shots), TA = 12:33 min for ETL = 1 and TA = 1:48 min for ETL = 7. Echo spacing and TE were slightly different for different types of pulse pairs as the minimum echo spacing depends on RF pulse duration, which differs among pulse pairs. For the CP modes and the 1-spoke LS-LS pulses, a sub-pulse with time-bandwidth product (TBW) of 4 and 2.5 ms of duration was used. For the 1-spoke MLS refocusing pulse, the sub-pulse length was increased to 3.2 ms as we observed that this improved uniformity performance (whereas for 1-spoke LS refocusing pulse, this did not change pulse performance). For 2-spoke pulses, a sub-pulse with TBW = 4 and 1.9 ms duration was used. The spoke locations were chosen to be (0,0,0) and (5,5,0).

2.6. Code availability

The SAR constrained arbitrary FA pulse design algorithm proposed in this work is available for download at https://github.com/filizyetisir/LFA_RFpulseDesign.

3. Results

3.1. Explicit local SAR constraints

Fig. 2 shows the trade-off between $|\beta^2|$ error (NRMMSE) and peak local SAR for the local SAR constrained 1-spoke and 2-spoke refocusing pulses for a duty cycle of 15%. Head average SAR, maximum average power per channel, total average power and maximum peak RF power per channel are also shown in Fig. 2. For reference, results for the CP mode of the coil are shown whereby pulses are scaled so that the average FA throughout the slice is equal to the target (CP mode average). Additionally, the local SAR vs $|\beta^2|$ error is shown for when a simple RF peak power constraint is used rather than the local SAR constraints. For a 32% refocusing uniformity error (marked with a black vertical dashed line), the explicit local SAR constrained design reduced pSAR10g by 56% and 54% compared to the CP mode (with matched RF duration) for 1- and 2-spoke pulses respectively. When the pSAR10g is chosen to be that of the CP mode of the coil (or below in case of 1-spoke pulses) the refocusing uniformity error is reduced by 41% and 59% respectively for

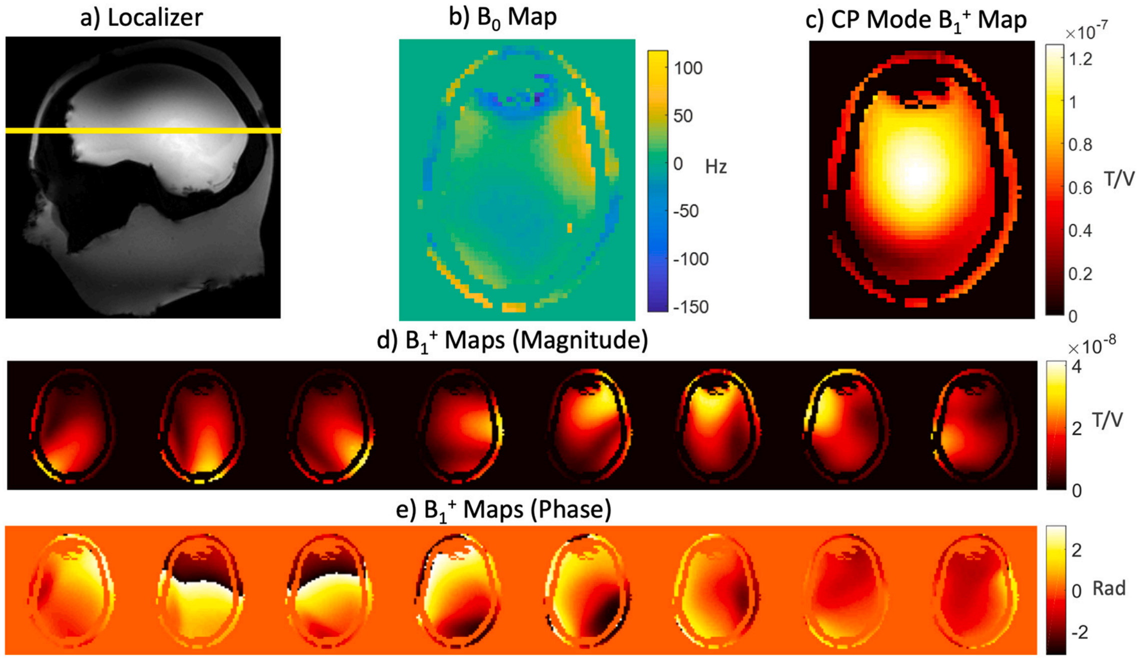

Fig. 1. a) Localizer image and the axial image slice location (yellow line) of the homogeneous anthropomorphic head phantom b) Off-resonance field map, c) CP mode B_1^+ map and d)/e) Magnitude/phase B_1^+ maps of each transmit channel of the in-house built 8 channel pTx array inside the imaging slice. (For interpretation of the references to colour in this figure legend, the reader is referred to the web version of this article.)

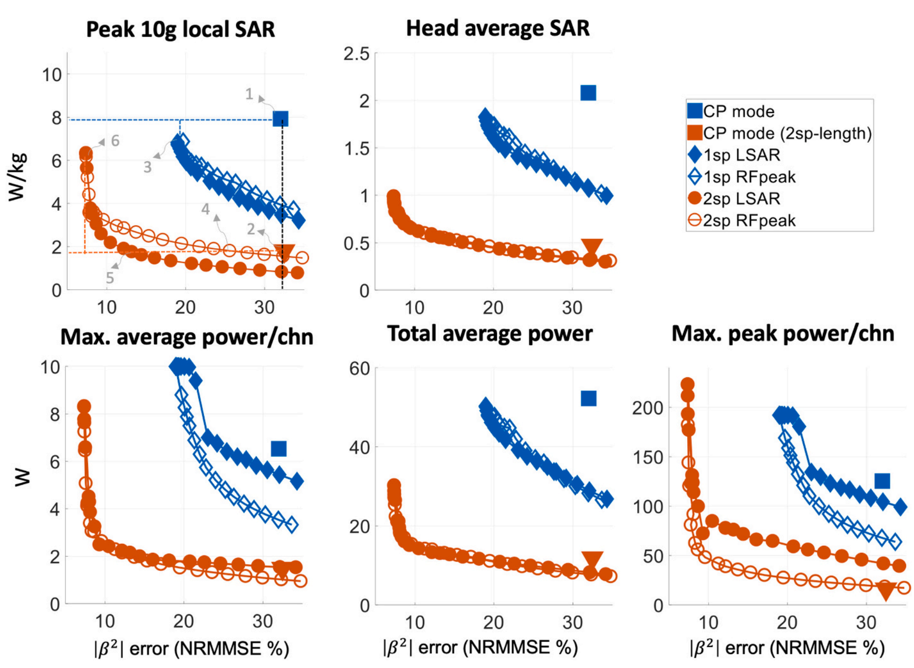

Fig. 2. L-curves demonstrating the trade-off between the refocusing uniformity ($|\beta^2|$) error versus peak 10 g local SAR, head average SAR, maximum average power per channel, total average power and maximum peak power per channel for CP mode and various pTx RF pulses. L-curves shown are for 1-spoke and 2-spoke, peak local SAR (LSAR) or RF peak voltage (RFpeak) constrained pTx pulses for a duty cycle of 15%. CP mode of the pTx array is also plotted for two different RF pulse lengths, matched to those of the 1-spoke or 2-spoke pulses (2sp-length). The CP mode pulses are scaled so that the average FA throughout the slice is equal to the target (CP mode average). Local SAR constrained pTx pulse design improves the refocusing uniformity vs local SAR trade-off compared to both the CP mode of the pTx array and the RF peak power constrained pTx pulse design. sp: spoke(s).

1- and 2-spoke pulses (blue and orange horizontal dashed lines). Using explicit local SAR constraints is an improvement over using peak power constraints for nearly all $|\beta^2|$ RMMSEs, especially for 2-spoke pulses. Converting from RF peak power constraints to local SAR constraints can reduce pSAR10g by up to 46% for the same refocusing uniformity error and reduce refocusing uniformity error by up to 52% for the same level of peak local SAR. Fig. 3 compares the $|\beta^2|$ profiles of pulses at points 1–6 shown in Fig. 2.

The same duty cycle (15%) is used to calculate SAR and power for all pulses in Fig. 2 for simplicity. If the same imaging sequence parameters are used for 1- and 2-spoke pulses, their duty cycles will be different because the pulse lengths are different. Supporting Information Fig. S3 shows SAR and power values shown in Fig. 2 when the imaging sequence parameters are the same for 1- and 2-spoke pulses resulting in a duty cycle of 15% and 29%, respectively. In this case, the peak local SAR, head average SAR and average power is scaled by approximately a factor of 2 for 2-spoke pulses. However, all SAR and power values are still lower for 2-spoke pulses compared to 1-spoke pulses for the same refocusing nonuniformity level.

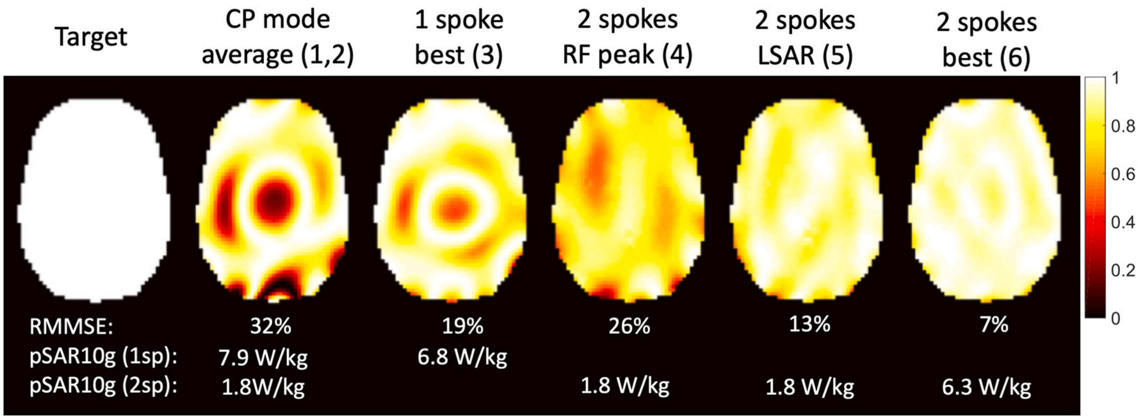

Fig. 3. Refocusing profiles ($|\beta^2|$) of different pulses shown in Fig. 2 (points 1–6). The point in Fig. 2 corresponding to each $|\beta^2|$ profile is shown in parenthesis. The CP mode results show the familiar constructive interference B_1^+ brightening in the center of the head and the associated "over-flipping" in this region when the FA is calibrated by a whole-slice average. The over-flipping at the bottom is due to the proximity of the head to the bottom of the coil. RMMSE and pSAR10g for each pulse is noted below its $|\beta^2|$ profile.

3.2. Computation time

Table 1 shows typical pulse computation times for 1-spoke or 2-spoke excitation and refocusing pulses designed with the LS and MLS approaches, respectively. Overall, providing the optimizer with the analytical Jacobian and (approximated) Hessian matrices computed using a GPU improved optimization time of the excitation-refocusing pulse pair by a factor of 32 and 76 for 1 and 2 spokes respectively compared to the CPU case with no analytical Jacobian or Hessian matrix. Using the GPU, providing the optimizer with the analytical expression of the Jacobian and the (approximated) Hessian matrices improved computation time of the excitation-refocusing pulse pair by a factor of 9 and 19 for 1 and 2 spokes, respectively. The reported computation times in Table 1 are for the large FA pulse design. The small tip angle approximation pulse design, carried out to initialize the large FA pulse design, took 0.4–0.6 s for excitation pulses using the LS and 2.5–2.7 s for refocusing pulses using the MLS approach.

3.3. Phantom imaging validations

Fig. 4 shows simulated excitation and refocusing profiles for the optimized pTx pulses as well as for the conventional CP modes (FA calibrated for the slice center and slice average) using the measured B_1^+ fields in an anthropomorphic head phantom. The CP mode results show the familiar constructive interference B_1^+ brightening in the center of the head and the associated "over-flipping" in this region when the FA is calibrated by a whole-slice average. The phase difference maps (between the excitation and the refocusing profiles) are also shown. These maps are a measure of how well the CPMG condition is satisfied by the excitation and refocusing pulse pair. Using pTx pulses designed with the proposed approach improved excitation uniformity by up to 78% and refocusing uniformity by up to 83% compared to the CP mode (average). Using the MLS approach in the optimization improved refocusing uniformity by 56% compared to the traditional LS approach. The 2-spoke MLS-LS pulse pair provided 25% better refocusing uniformity and 45% better excitation uniformity compared to the next best results, the 1-spoke MLS-LS pulse pair. The CPMG condition for each type of pulse pair is also improved by the pTx pulses. Note that for the CP mode, off-resonance effects lead to deviations from the ideal phase difference between the excitation and refocusing pulse pair. 1-spoke and 2-spoke pulse pairs mitigate this effect to some extent.

Simulated spin echo signal profiles for different excitation-refocusing pulse pairs are shown in Fig. 5. Top and bottom rows show the simulated spin echo signal without slice profile effects (simulated only at z = 0 mm) and with slice profile effects (simulated at 41 points between z = [−8 mm, 8 mm] and the signal at all z points summed), respectively. Slice profile across the slice select direction for different pulses are plotted for all in plane locations in Supporting Information Fig. S4. Average slice profile errors across the transverse plane for 90° excitation pulses are comparable with those of 30° excitation pulses (0.98–1.16 for 90° excitation pulses vs 1.04–1.07 for 30° excitation pulses) whereas the average slice profile error for 180° refocusing pulses are higher (1.32–1.81), see Supporting Information Fig. S5. The average and the standard deviation of slice profile errors for 90° excitation pulses are similar among CP mode, 1- spoke and 2-spoke pulses, except they are higher for the CP mode average pulse due to the effects of over flipping. The average slice profile error of refocusing pulses is lower for the 2-spoke case (1.32) compared to the CP mode (1.50–1.81) and 1-spoke (1.69–1.72) cases. However, note that this difference is mainly due to 2-spoke pulses having a shorter sub-pulse duration (1.9 ms) compared to CP mode and 1-spoke pulses (2.5–3.2 ms), and thus having smaller offsets and smearing in the slice profile due to off resonance and VERSE effects. On the other hand, the normalized standard deviation of the slice profile error (normalized by the mean) of refocusing pulses is higher for

Table 1
Large FA pulse design times for typical 1-spoke and 2-spoke excitation pulses designed using the LS approach, and for typical 1-spoke and 2-spoke refocusing pulses designed using the MLS approach. The computation times are in seconds. J: analytical Jacobian, H: approximated analytical Hessian, ✓/× computed/not computed for the optimization.

		1 spoke		2 spokes	
		90° Excitation (LS)	180° Refocusing (MLS)	90° Excitation (LS)	180° Refocusing (MLS)
J (×)	CPU	3.0	74.2	97.4	470.5
H (×)	GPU	0.9	21.8	25.8	116.0
J (✓)	CPU	6.5	217.0	127.5	534.6
H (×)	GPU	0.4	7.8	4.4	16.4
J (✓)	CPU				
H (✓)	GPU	0.2	2.2	2.0	5.5

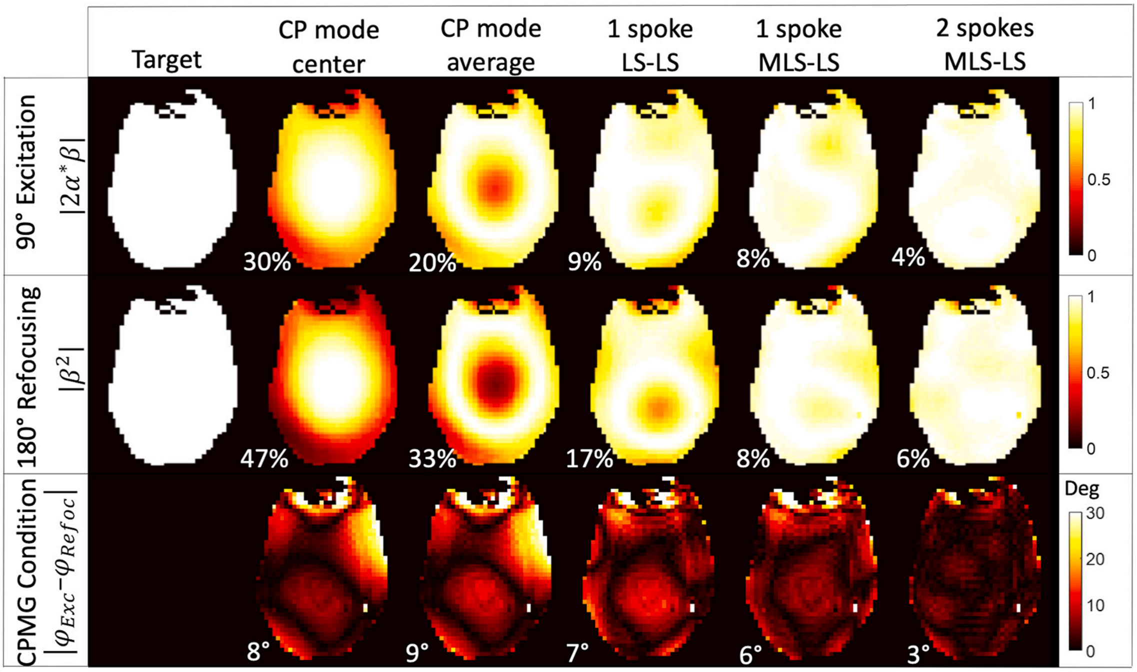

Fig. 4. First and second row: simulated excitation and refocusing profiles (magnitude) of CP mode and pTx pulses in the head phantom. NRMMSEs are reported on the lower left corner. Third row: The phase difference map between the excitation and refocusing profiles. Mean values of the phase difference maps are noted on the lower left corner. Second and third columns: for the CP mode, the pulse is scaled to achieve the target FA in the center of the slice or on average across the slice. Fourth column: both excitation and refocusing pulses are designed using the LS approach. Fifth and sixth columns: refocusing pulse (1 or 2 spokes) is designed using the MLS approach whereas the excitation pulse (1 or 2 spokes) is designed using the LS approach.

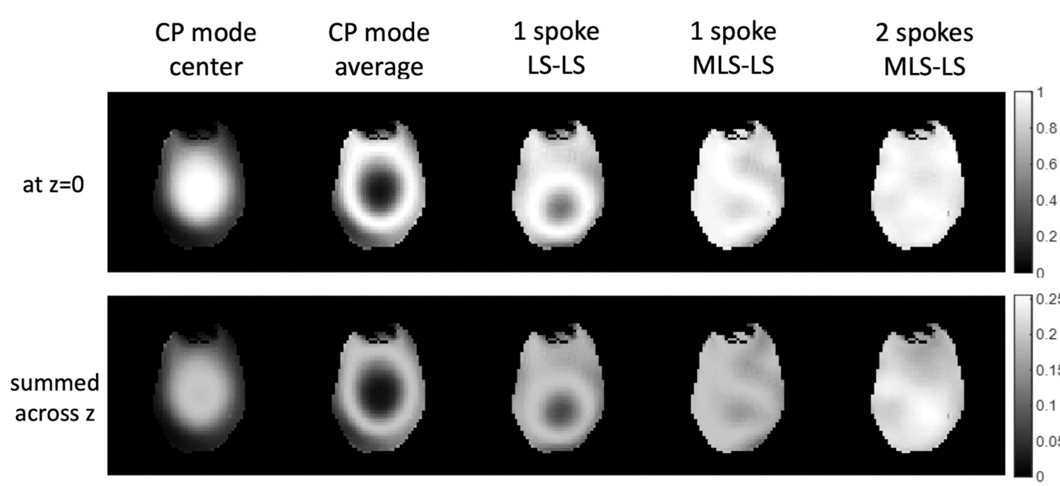

Fig. 5. Simulated spin echo signal for different excitation-refocusing pulse pairs simulated without slice profile effects (top row) and with slice profile effects (bottom row). z: slice select direction.

2-spoke case (21%) compared to CP mode (7% for center, 20% for average) and 1-spoke (6%–12%) cases.

Fig. 6 shows the imaging results when the designed pulses are applied to the anthropomorphic head phantom. The optimized pTx pulse pairs significantly improve image shading in the single spin echo and RARE images compared to the CP mode. Additionally, image shading patterns observed in Fig. 5 are in good agreement with that expected from the simulated profiles in the second row of Fig. 5. Note that the receive profile was not removed from these images via post-processing. Fig. 6 also shows a difference image between the single spin echo and the RARE image for each pulse pair in order to estimate image artifacts introduced by the repeated application of the refocusing pulses. These difference images in the third row in Fig. 6 show that the artifact level in the RARE images for pTx pulses is comparable to the artifact level for the CP mode.

4. Discussion

Incorporating explicit local SAR constraints in the pTx pulse design can simultaneously reduce excitation or refocusing uniformity and peak local SAR compared to the CP mode. For refocusing pulses, which dominate the SAR in a RARE sequence, the proposed pulse design approach reduced pSAR10g by up to 56% and mitigated transmit field inhomogeneity by up to 59% compared to CP mode for a single slice in a simulated dataset. Our approach has several advantages over the previous large FA pulse design approaches which constrain SAR by constraining RF peak power. First, it results in more optimal RF pulses in terms of the excitation and refocusing uniformity versus pSAR10g trade

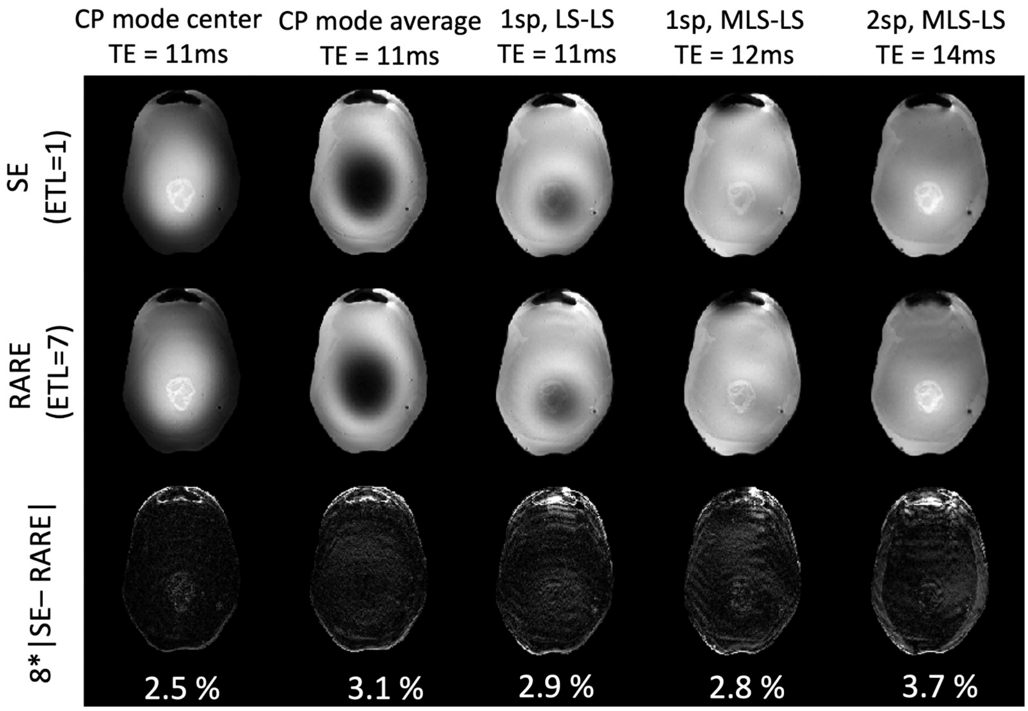

Fig. 6. Single spin echo (SE, first row) and RARE (second row) images obtained using the excitation and refocusing pulses designed in Fig. 3. Differences of SE and RARE images (third row, amplified by a factor of 8) show the artifacts introduced due to repeated application of refocusing pulses to speed up imaging. The mean artifact levels (normalized by the signal level in the corresponding SE image) are noted at the bottom, which were calculated using Eq. (6). Note that the FFT factor for image reconstruction was reduced for 2-spoke images due to signal saturation at the center, hence the overall signal level is slightly lower than the CP mode and 1-spoke images. The receive profile was not removed from the images via post-processing. ETL: echo train length, sp: spoke(s).

off (up to 46% less pSAR10g or up to 52% less uniformity error) which is in agreement with previous findings in the small FA domain [32]. Second, for RF power constrained approaches, it may take several attempts to find which RF peak power level will correspond to a given local SAR limit. Hence, the proposed approach eliminates the trial-and-error step to satisfy the regulatory limits. Finally, by applying the VERSE algorithm prior to pulse design, the re-optimization step after the pulse design (to correct for the off-resonance effects introduced by the VERSE algorithm) is eliminated.

Previous studies implementing different approaches to design slice selective large FA pulses point out the computational burden of including local SAR constraints into the pulse design [52,61]. Similarly, for the approach taken in this study, running a full numerical simulation of the Bloch equations at every iteration and introducing hundreds of local SAR constraints into the minimization resulted in long computation times, i.e., 77 s and 568 s for 1- and 2-spoke excitation-refocusing pulse pairs. In order to address this issue, we provided the minimizer with the analytical expressions for the Jacobian and the approximated Hessian matrices, computed using a GPU, and reduced computation time for the large flip angle algorithm by up to a factor of 76 for the excitation-refocusing pulse pairs we designed. The total computation time (for a single slice, together with the small tip angle approximation pulse design for the initialization) was 5.5 s and 10.6 s per pulse pair for 1 and 2 spokes respectively. Note that for multi-slice imaging, the pulse design for each slice can be carried out in parallel given sufficient parallel computation resources.

Given the same pulse lengths, a refocusing pulse is more challenging to design and demands more power than an excitation pulse. Hence, the refocusing pulse was designed first using an MLS approach, followed by the excitation pulse designed using the LS approach with the CPMG-preserving phase target calculated from the refocusing pulse. An alternative approach to the sequential design of the refocusing-excitation pulse pair is to jointly design the pulse pair, optimizing not the individual phase profiles but the phase difference to enforce the CPMG condition [60]. This might improve the pulse performance compared to our method. Another alternative approach is to combine our proposed method with methods optimizing the signal intensity along the echo train and thus eliminating the need to explicitly enforce the CPMG condition in pulse design [61,75,76]. This approach is likely to improve the pulse performance at the expense of increased computation time.

In this study, windowed and VERSEd sinc sub-pulses were used to design excitation and refocusing pulses. The deviation of the slice profile from an ideal rectangular slice profile for 90° excitation pulses was similar to that of small tip angle (FA = 30°) excitation pulses whereas it was worse for refocusing pulses (FA = 180°). This result is expected as the violation of the small tip angle approximation is more significant for refocusing pulses. Moreover, the degradation in the slice profile due to violation of the small tip angle approximation was less uniform across the transverse plane for the 2-spoke spin echo signal compared to the CP mode and 1-spoke spin echo signals (shown in Supporting Information Fig. S5), the effect of which can be seen in Fig. 5. One approach to improve the slice profile, especially for CP mode and 1-spoke pulses, is to use SLR sub-pulses [63] instead of windowed sinc sub-pulses. For multi-spoke pulses however, the slice profile is likely to be degraded compared to the single spoke case when using SLR sub-pulses, similarly to when using sinc sub-pulses.

The pTx pulses designed using the proposed approach were validated in phantom experiments with PD-weighted and T_2-weighted RARE imaging. The designed pTx pulses significantly reduced image shading in the phantom. The simulated spin echo signal profiles were in good agreement with the experimental image shading. Note that some mismatch between the simulated and experimental image shading might be caused by the receive profile which was not removed from the SE and RARE images. For 2-spoke pulses, we observed some artifacts at the top of the phantom where the phantom gel was degraded and was replaced by air over time. Hence, these artifacts are likely caused by the inaccurate off resonance field mapping in this region and the sensitivity of 2-spoke pulses to the off-resonance field imperfections.

A duty cycle of 15% was assumed when calculating the local SAR, global SAR and average power in this study. If the same imaging parameters are used as the 1-spoke pulses, the duty cycle for the 2-spoke pulses would be 29%. As an example, a RARE imaging protocol with a TR of 7 s, echo train length of 9 and 45 slices would result in a duty cycle of 15% for 1-spoke and 29% for 2-spoke pulses designed in this study. As shown in Supporting Information Fig. S3, almost all pulses result in pSAR10g, head average SAR, average power and peak power levels below the regulatory and hardware limits, indicating the extendibility of the current work to multi-slice imaging. For higher duty cycles or when slices which require higher RF power are included, pSAR10g and average power per channel might be limiting factors. However, the target refocusing flip angle for the designed pulses (chosen to be the maximum possible, i.e., 180°, in this work) can be reduced to overcome this limitation (SAR scales with the square of the flip angle) as is usually done in clinical imaging protocols in CP mode.

In the current study, spoke locations were not optimized. However, for multi-slice in-vivo imaging, pulse performance can significantly benefit from spoke location optimization [52,55]. In that case, the gradient blips can be parametrized and optimized at the expense of increased computation time. On the other hand, the computation time can be reduced by replacing the rotation matrix calculations by an analytical approximation derived from Average Hamiltonian Theory, which was shown to significantly reduce the computational burden for 2- and 3-spoke 90° excitation pulses [55].

5. Conclusion

This study implemented a spinor-based pTx pulse design algorithm with explicit local SAR constraints to design slice selective RF pulses for 2D RARE imaging. Using this algorithm, refocusing pulses were designed using a magnitude least squares approach followed by a least-squares design of the excitation pulse accompanied by the target phase needed to satisfy the CPMG condition. The pulse computation times were reduced by up to a factor of 76 (down to 6 s – 11 s for a single excitation-refocusing pulse pair) by implementing parallel computation and providing the optimizer with analytical expressions of the Jacobian and the approximated Hessian matrices. On a simulated dataset, the designed pulses resulted in significantly reduced pSAR10g (up to 56%), and uniformity error (up to 59%) compared to CP mode. The designed pulses were validated through phantom experiments in a single slice. Good agreement between predicted and experimental image shading patterns was observed. Future work will include extension to and demonstration for multi-slice in-vivo imaging.

CRediT authorship contribution statement

Filiz Yetisir: Conceptualization, Methodology, Software, Investigation, Writing – original draft, Visualization. **Benedikt A. Poser:** Software, Investigation, Resources. **P. Ellen Grant:** Resources, Funding acquisition. **Elfar Adalsteinsson:** Conceptualization, Resources, Writing – review & editing, Supervision, Funding acquisition. **Lawrence L. Wald:** Conceptualization, Resources, Writing – review & editing, Supervision, Funding acquisition. **Bastien Guerin:** Conceptualization, Methodology, Software, Writing – review & editing.

Declaration of Competing Interest

None.

Acknowledgements

This work was supported by National Institutes of Health (R01EB006847, R01EB017337, U01HD087211, P41EB015896, R01MH111444), Netherlands Organization for Scientific Research (NWO VIDI 016.178.052) and Siemens MR.

Appendix A. Supplementary data

Supplementary data to this article can be found online at https://doi.org/10.1016/j.mri.2022.08.006.

References

[1] Uğurbil K. Magnetic Resonance Imaging at Ultrahigh Fields. IEEE Trans Biomed Eng 2014;61:1364–79. https://doi.org/10.1109/TBME.2014.2313619.
[2] Ladd ME, Bachert P, Meyerspeer M, Moser E, Nagel AM, Norris DG, et al. Pros and cons of ultra-high-field MRI/MRS for human application. Prog Nucl Magn Reson Spectrosc 2018;109:1–50. https://doi.org/10.1016/j.pnmrs.2018.06.001.
[3] Balchandani P, Naidich TP. Ultra-high-field MR neuroimaging. Am J Neuroradiol 2015;36:1204–15. https://doi.org/10.3174/ajnr.A4180.
[4] van der Kolk AG, Hendrikse J, Zwanenburg JJM, Visser F, Luijten PR. Clinical applications of 7T MRI in the brain. Eur J Radiol 2013;82:708–18. https://doi.org/10.1016/j.ejrad.2011.07.007.
[5] Springer E, Dymerska B, Cardoso PL, Robinson SD, Weisstanner C, Wiest R, et al. Comparison of Routine Brain Imaging at 3 T and 7 T. Invest Radiol 2016;51:469–82. https://doi.org/10.1097/RLI.0000000000000256.
[6] Trattnig S, Springer E, Bogner W, Hangel G, Strasser B, Dymerska B, et al. Key clinical benefits of neuroimaging at 7 T. NeuroImage 2018;168:477–89. https://doi.org/10.1016/j.neuroimage.2016.11.031.
[7] Kraff O, Quick HH. 7T: Physics, safety, and potential clinical applications. J Magn Reson Imaging 2017;46:1573–89. https://doi.org/10.1002/jmri.25723.
[8] Vaughan JT, Garwood M, Collins CM, Liu W, DelaBarre L, Adriany G, et al. 7T vs. 4T: RF power, homogeneity, and signal-to-noise comparison in head images. Magn Reson Med 2001;46:24–30. https://doi.org/10.1002/mrm.1156.
[9] Moortele P, Akgun C, Adriany G, Moeller S, Ritter J, Collins CM, et al. B1 destructive interferences and spatial phase patterns at 7 T with a head transceiver array coil. Magn Reson Med 2005;54:1503–18. https://doi.org/10.1002/mrm.20708.
[10] Fiedler TM, Ladd ME, Bitz AK. SAR Simulations & Safety. Neuroimage 2018;168:33–58. https://doi.org/10.1016/j.neuroimage.2017.03.035.
[11] Hennig J, Nauerth A, Friedburg H. RARE imaging: A fast imaging method for clinical MR. Magn Reson Med 1986;3:823–33. https://doi.org/10.1002/mrm.1910030602.
[12] Conolly S, Pauly J, Nishimura D, Macovsiu A. Two-dimensional selective adiabatic pulses. Magn Reson Med 1992;24:302–13. https://doi.org/10.1002/mrm.1910240211.
[13] Balchandani P, Pauly J, Spielman D. Slice-selective Tunable-flip AdiaBatic Low peak-power Excitation (STABLE) pulse. Magn Reson Med 2008;59:1072–8. https://doi.org/10.1002/mrm.21540.
[14] Balchandani P, Glover G, Pauly J, Spielman D. Improved slice-selective adiabatic excitation. Magn Reson Med 2014;71:75–82. https://doi.org/10.1002/mrm.24630.
[15] Garwood M, Uğurbil K. RF pulse methods for use with surface coils: Frequency-modulated pulses and parallel transmission. J Magn Reson 2018;291:84–93. https://doi.org/10.1016/j.jmr.2018.01.012.
[16] Mullen M, Kobayashi N, Garwood M. Two-dimensional frequency-swept pulse with resilience to both B1 and B0 inhomogeneity. J Magn Reson 2019;299:93–100. https://doi.org/10.1016/j.jmr.2018.12.017.
[17] Conolly S, Nishimura D, Macovski A, Glover G. Variable-rate selective excitation. J Magn Reson 1988;78:440–58. https://doi.org/10.1016/0022-2364(88)90131-X.
[18] Hennig J, Scheffler K. Hyperechoes. Magn Reson Med 2001;46:6–12. https://doi.org/10.1002/mrm.1153.
[19] Hennig J, Weigel M, Scheffler K. Multiecho sequences with variable refocusing flip angles: Optimization of signal behavior using smooth transitions between pseudo steady states (TRAPS). Magn Reson Med 2003;49:527–35. https://doi.org/10.1002/mrm.10391.
[20] Foo TK, Hayes CE, Kang YW. Reduction of RF penetration effects in high field imaging. Magn Reson Med 1992;23:287–301. https://doi.org/10.1002/mrm.1910230209.
[21] Yang QX, Mao W, Wang J, Smith MB, Lei H, Zhang X, et al. Manipulation of image intensity distribution at 7.0 T: Passive RF shimming and focusing with dielectric material. J Magn Reson Imaging 2006;24:197–202. https://doi.org/10.1002/jmri.20603.
[22] Webb A, g.. Dielectric materials in magnetic resonance. Concepts Magn Reson Part A 2011;38A:148–84. https://doi.org/10.1002/cmr.a.20219.
[23] Haines K, Smith NB, Webb AG. New high dielectric constant materials for tailoring the B1+ distribution at high magnetic fields. J Magn Reson 2010;203:323–7. https://doi.org/10.1016/j.jmr.2010.01.003.
[24] O'Reilly TPA, Webb AG, Brink WM. Practical improvements in the design of high permittivity pads for dielectric shimming in neuroimaging at 7T. J Magn Reson San Diego Calif 1997;2016(270):108–14. https://doi.org/10.1016/j.jmr.2016.07.003.
[25] Sengupta S, Roebroeck A. Dielectric pads for high-field MRI at 7T: a simulation study. In: Proc. 26th Annu. Meet. ISMRM, Paris, France; 2018. p. 4307.
[26] van Gemert J, Brink W, Remis R, Webb A. A simulation study on the effect of optimized high permittivity materials on fetal imaging at 3T. Magn Reson Med 2019;82:1822–31. https://doi.org/10.1002/mrm.27849.
[27] Katscher U, Börnert P, Leussler C, Brink JS. Transmit SENSE. Magn Reson Med 2003;49:144–50. https://doi.org/10.1002/mrm.10353.
[28] Zhu Y. Parallel excitation with an array of transmit coils. Magn Reson Med 2004;51:775–84. https://doi.org/10.1002/mrm.20011.
[29] Adriany G, Van de Moortele P-F, Wiesinger F, Moeller S, Strupp JP, Andersen P, et al. Transmit and receive transmission line arrays for 7 Tesla parallel imaging. Magn Reson Med 2005;53:434–45. https://doi.org/10.1002/mrm.20321.
[30] Orzada S, Maderwald S, Poser BA, Bitz AK, Quick HH, Ladd ME. RF excitation using time interleaved acquisition of modes (TIAMO) to address B1 inhomogeneity in high-field MRI. Magn Reson Med 2010;64:327–33. https://doi.org/10.1002/mrm.22527.

[31] Setsompop K, Wald LL, Alagappan V, Gagoski BA, Adalsteinsson E. Magnitude least squares optimization for parallel radio frequency excitation design demonstrated at 7 Tesla with eight channels. Magn Reson Med 2008;59:908–15. https://doi.org/10.1002/mrm.21513.
[32] Guérin B, Gebhardt M, Cauley S, Adalsteinsson E, Wald LL. Local specific absorption rate (SAR), global SAR, transmitter power, and excitation accuracy trade-offs in low flip-angle parallel transmit pulse design. Magn Reson Med 2014;71:1446–57. https://doi.org/10.1002/mrm.24800.
[33] Davids M, Schad LR, Wald LL, Guérin B. Fast three-dimensional inner volume excitations using parallel transmission and optimized k-space trajectories. Magn Reson Med 2016;76:1170–82. https://doi.org/10.1002/mrm.26021.
[34] Ianni JD, Cao Z, Grissom WA. Machine learning RF shimming: Prediction by iteratively projected ridge regression. Magn Reson Med 2018;80:1871–81. https://doi.org/10.1002/mrm.27192.
[35] Tomi-Tricot R, Gras V, Thirion B, Mauconduit F, Boulant N, Cherkaoui H, et al. SmartPulse, a machine learning approach for calibration-free dynamic RF shimming: Preliminary study in a clinical environment. Magn Reson Med 2019;82:2016–31. https://doi.org/10.1002/mrm.27870.
[36] Mao X, Vike NL, Talavage TM, Rispoli JV, Love DJ. Multiple-Input Multiple-Output (MIMO) MRI: Combining Parallel Excitation and Parallel Reception for Enhanced Imaging. IEEE Trans Comput Imaging 2019;5:596–605. https://doi.org/10.1109/tci.2019.2904882.
[37] Pendse M, Stara R, Mehdi Khalighi M, Rutt B. IMPULSE: A scalable algorithm for design of minimum specific absorption rate parallel transmit RF pulses. Magn Reson Med 2019;81:2808–22. https://doi.org/10.1002/mrm.27589.
[38] Ma J, Gruber B, Yan X, Grissom WA. k-Space Domain Parallel Transmit Pulse Design. Magn Reson Med 2021;85:2568–79. https://doi.org/10.1002/mrm.28601.
[39] Herrler J, Liebig P, Gumbrecht R, Ritter D, Schmitter S, Maier A, et al. Fast online-customized (FOCUS) parallel transmission pulses: A combination of universal pulses and individual optimization. Magn Reson Med 2021;85:3140–53. https://doi.org/10.1002/mrm.28643.
[40] Damme LV, Mauconduit F, Chambrion T, Boulant N, Gras V. Universal nonselective excitation and refocusing pulses with improved robustness to off-resonance for Magnetic Resonance Imaging at 7 Tesla with parallel transmission. Magn Reson Med 2021;85:678–93. https://doi.org/10.1002/mrm.28441.
[41] Hoyos-Idrobo A, Weiss P, Massire A, Amadon A, Boulant N. On Variant Strategies to Solve the Magnitude Least Squares Optimization Problem in Parallel Transmission Pulse Design and Under Strict SAR and Power Constraints. IEEE Trans Med Imaging 2014;33:739–48. https://doi.org/10.1109/TMI.2013.2295465.
[42] Yetisir F, Guerin B, Wald LL, Adalsteinsson E. Local and global SAR constrained large tip angle 3D kt points parallel transmit pulse design at 7 T. In: Proc. 22nd Annu. Meet. ISMRM, Milan, Italy; 2014. p. 1454.
[43] Massire A, Vignaud A, Robert B, Le Bihan D, Boulant N, Amadon A. Parallel-transmission-enabled three-dimensional T2-weighted imaging of the human brain at 7 Tesla. Magn Reson Med 2015;73:2195–203. https://doi.org/10.1002/mrm.25353.
[44] Gras V, Vignaud A, Amadon A, Le Bihan D, Boulant N. Universal pulses: A new concept for calibration-free parallel transmission. Magn Reson Med 2017;77:635–43. https://doi.org/10.1002/mrm.26148.
[45] Gras V, Mauconduit F, Vignaud A, Amadon A, Bihan DL, Stöcker T, et al. Design of universal parallel-transmit refocusing kT-point pulses and application to 3D T2-weighted imaging at 7T. Magn Reson Med 2018;80:53–65. https://doi.org/10.1002/mrm.27001.
[46] Massire A, Cloos MA, Vignaud A, Le Bihan D, Amadon A, Boulant N. Design of non-selective refocusing pulses with phase-free rotation axis by gradient ascent pulse engineering algorithm in parallel transmission at 7T. J Magn Reson 2013;230:76–83. https://doi.org/10.1016/j.jmr.2013.01.005.
[47] Jang A, Wu X, Auerbach EJ, Garwood M. Designing 3D selective adiabatic radiofrequency pulses with single and parallel transmission. Magn Reson Med 2018;79:701–10. https://doi.org/10.1002/mrm.26720.
[48] Li Q, Liao C, Ye H, Chen Y, Cao X, Yuan L, et al. Squeezed Trajectory Design for Peak RF and Integrated RF Power Reduction in Parallel Transmission MRI. IEEE Trans Med Imaging 2018;37:1809–21. https://doi.org/10.1109/TMI.2018.2828112.
[49] Vinding MS, Guérin B, Vosegaard T, Nielsen NC. Local SAR, global SAR, and power-constrained large-flip-angle pulses with optimal control and virtual observation points. Magn Reson Med 2017;77:374–84. https://doi.org/10.1002/mrm.26086.
[50] Malik SJ, Hajnal JV. Phase relaxed localized excitation pulses for inner volume fast spin echo imaging. Magn Reson Med 2016;76:848–61. https://doi.org/10.1002/mrm.25996.
[51] Grissom WA, Yip C-Y, Wright SM, Fessler JA, Noll DC. Additive angle method for fast large-tip-angle RF pulse design in parallel excitation. Magn Reson Med 2008;59:779–87. https://doi.org/10.1002/mrm.21510.
[52] Cao Z, Donahue MJ, Ma J, Grissom WA. Joint design of large-tip-angle parallel RF pulses and blipped gradient trajectories. Magn Reson Med 2016;75:1198–208. https://doi.org/10.1002/mrm.25739.
[53] Carr HY, Purcell EM. Effects of Diffusion on Free Precession in Nuclear Magnetic Resonance Experiments. Phys Rev 1954;94:630–8. https://doi.org/10.1103/PhysRev.94.630.
[54] Meiboom S, Gill D. Modified Spin-Echo Method for Measuring Nuclear Relaxation Times. Rev Sci Instrum 1958;29:688–91. https://doi.org/10.1063/1.1716296.
[55] Gras V, Vignaud A, Amadon A, Mauconduit F, Bihan DL, Boulant N. In vivo demonstration of whole-brain multislice multispoke parallel transmit radiofrequency pulse design in the small and large flip angle regimes at 7 Tesla. Magn Reson Med 2017;78:1009–19. https://doi.org/10.1002/mrm.26491.
[56] Setsompop K, Alagappan V, Zelinski AC, Potthast A, Fontius U, Hebrank F, et al. High-Flip-Angle slice-selective parallel RF transmission with 8 channels at 7 Tesla. J Magn Reson 2008;195:76–84. https://doi.org/10.1016/j.jmr.2008.08.012.
[57] Wu X, Auerbach EJ, Vu AT, Moeller S, Lenglet C, Schmitter S, et al. High-resolution whole-brain diffusion MRI at 7T using radiofrequency parallel transmission. Magn Reson Med 2018;80:1857–70. https://doi.org/10.1002/mrm.27189.
[58] Ding B, Dragonu I, Liebig P, Heidemann RM, Rodgers CT. Dynamic parallel transmission for diffusion MRI at 7T. In: Proc. 28th Annu. Meet. ISMRM, Virtual; 2021. p. 1313.
[59] Williams SN, Dragonu I, Liebig P, Porter DA. Multi-Slice 2D pTx Readout-Segmented Diffusion-Weighted Imaging Using Slice-by-Slice B1+ Shimming. In: Proc. 28th Annu. Meet. ISMRM, Virtual; 2021. p. 4176.
[60] Xu D, King KF. Joint Design of Excitation and Refocusing Pulses for Fast Spin Echo Sequences in Parallel Transmission. In: Proc. 17th Annu. Meet. Honolulu, Hawai'i, USA: ISMRM; 2009. p. 174.
[61] Sbrizzi A, Hoogduin H, Hajnal JV, van den Berg CAT, Luijten PR, Malik SJ. Optimal control design of turbo spin-echo sequences with applications to parallel-transmit systems. Magn Reson Med 2017;77:361–73. https://doi.org/10.1002/mrm.26084.
[62] Yetisir F, Guerin B, Poser BA, Wald LL, Adalsteinsson E. Impact of RF-shimming on the uniformity and specific absorption rate of spin-echo imaging at 7 Tesla. In: Proc. 23rd Annu. Meet. Toronto, Ontario, Canada: ISMRM; 2015. p. 0920.
[63] Pauly J, Roux PL, Nishimura D, Macovski A. Parameter relations for the Shinnar-Le Roux selective excitation pulse design algorithm. IEEE Trans Med Imaging 1991;10:53–65. https://doi.org/10.1109/42.75611.
[64] Eichfelder G, Gebhardt M. Local specific absorption rate control for parallel transmission by virtual observation points. Magn Reson Med 2011;66:1468–76. https://doi.org/10.1002/mrm.22927.
[65] Saekho S, Boada FE, Noll DC, Stenger VA. Small tip angle three-dimensional tailored radiofrequency slab-select pulse for reduced B1 inhomogeneity at 3 T. Magn Reson Med 2005;53:479–84. https://doi.org/10.1002/mrm.20358.
[66] Setsompop K, Wald LL, Alagappan V, Gagoski B, Hebrank F, Fontius U, et al. Parallel RF transmission with eight channels at 3 Tesla. Magn Reson Med 2006;56:1163–71. https://doi.org/10.1002/mrm.21042.
[67] Wu X, Adriany G, Ugurbil K, Van de Moortele P-F. Correcting for Strong Eddy Current Induced B0 Modulation Enables Two-Spoke RF Pulse Design with Parallel Transmission: Demonstration at 9.4T in the Human Brain. PLoS ONE 2013;8:e78078. https://doi.org/10.1371/journal.pone.0078078.
[68] Tse DHY, Wiggins CJ, Poser BA. Estimating and eliminating the excitation errors in bipolar gradient composite excitations caused by radiofrequency-gradient delay: Example of bipolar spokes pulses in parallel transmission. Magn Reson Med 2017;78:1883–90. https://doi.org/10.1002/mrm.26586.
[69] Gras V, Vignaud A, Amadon A, Mauconduit F, Bihan DL, Boulant N. New method to characterize and correct with sub-μs precision gradient delays in bipolar multispoke RF pulses. Magn Reson Med 2017;78:2194–202. https://doi.org/10.1002/mrm.26614.
[70] Pauly J, Nishimura D, Macovski A. A k-space analysis of small-tip-angle excitation. J Magn Reson 1989;81:43–56. https://doi.org/10.1016/0022-2364(89)90265-5.
[71] Fautz H-P, Vogel M, Gross P, Kerr A, Zhu Y. B1 mapping of coil arrays for parallel transmission. In: Proc. 16th Annu. Meet. ISMRM, Toronto, Ontario, Canada; 2008. p. 1247.
[72] Schneider E, Glover G. Rapid in vivo proton shimming. Magn Reson Med 1991;18:335–47. https://doi.org/10.1002/mrm.1910180208.
[73] Webb P, Macovski A. Rapid, fully automatic, arbitrary-volume in vivo shimming. Magn Reson Med 1991;20:113–22. https://doi.org/10.1002/mrm.1910200112.
[74] Guérin B, Stockmann JP, Baboli M, Torrado-Carvajal A, Stenger AV, Wald LL. Robust time-shifted spoke pulse design in the presence of large B0 variations with simultaneous reduction of through-plane dephasing, B1+ effects, and the specific absorption rate using parallel transmission. Magn Reson Med 2016;76:540–54. https://doi.org/10.1002/mrm.25902.
[75] Le Roux P. Non-CPMG Fast Spin Echo with Full Signal. J Magn Reson 2002;155:278–92. https://doi.org/10.1006/jmre.2002.2523.
[76] Lee S-K, Vogel MW, Grissom WA, Mckinnon GC, Roux PHL. Fast Spin Echo Imaging with Quadratic Phase-Modulated non-CPMG Echo Train in Parallel Transmit – a Simulation Study. In: Proc. 19th Annu. Meet. Montreal, Quebec, Canada: ISMRM; 2011. p. 4447.